Bulletin of the Seismological Society of America, Vol. XX, No. XX, pp. –, – 2018, doi: 10.1785/0120180037

Ⓔ

Magnitude Scales for Marsquakes

by Maren Böse,* Domenico Giardini, Simon Stähler, Savas Ceylan, John Francis Clinton, Martin van Driel, Amir Khan, Fabian Euchner, Philippe Lognonné, and William Bruce Banerdt

Abstract In anticipation of the upcoming 2018 InSight (Interior exploration using Seismic Investigations, Geodesy and Heat Transport) Discovery mission to Mars, we calibrate magnitude scales for marsquakes that incorporate state-of-the-art knowledge on Mars interior structure and the expected ambient and instrumental noise. We regress magnitude determinations of 2600 randomly distributed marsquakes, simulated with a spectral element method for 13 published 1D structural models of Mars' interior. The continuous seismic data from InSight will be returned at 2 samples per second. To account for this limited bandwidth as well as for the expected noise conditions on Mars, we define and calibrate six magnitude scales: (1) local Mars magnitude $M_{\mathrm{L}}^{\mathrm{Ma}}$ at a period of 3 s for marsquakes at distances of up to 10°; (2) P-wave magnitude $m_{\mathrm{b}}^{\mathrm{Ma}}$; (3) S-wave magnitude $m_{\mathrm{b}S}^{\mathrm{Ma}}$ each defined at a period of 3 s and calibrated for distances from 5° to 100°; (4) surface-wave magnitude $M_{\mathrm{s}}^{\mathrm{Ma}}$ defined at a period of 20 s, as well as (5) moment magnitudes $M_{\mathrm{FB}}^{\mathrm{Ma}}$; and (6) $M_{\mathrm{F}}^{\mathrm{Ma}}$ computed from the low-frequency (10–100 s) plateau of the displacement spectrum for either body waves or body and surface waves, respectively; we calibrate scales (4)–(6) for distances from 5° to 180°. We regress stable calibrations of the six scales with respect to the seismic moment magnitude at M_{w} 5.5 by correcting filtered phase amplitudes for attenuation with distance and source depth. Expected errors in epicentral distance and in source depth (25% and 20 km, respectively) translate into magnitude errors of 0.1–0.3 units. We validate our magnitude relations with an independent test dataset of 2600 synthetic marsquakes ($1.0 \leq M_{\mathrm{w}} \leq 7.0$), for which seismograms are superimposed on the realistic noise predicted by the InSight noise model. Marsquakes with $M_{\mathrm{w}} < 3.0$ and epicentral distances of $\Delta > 15°$ are expected to be hidden in the Mars background noise and will likely not be detectable.

Electronic Supplement: Figures showing preprocessing steps for amplitude and magnitude regression for Mars and results for Earth using the preliminary reference Earth model (PREM).

Introduction

The National Aeronautics and Space Administration (NASA) InSight (Interior exploration using Seismic Investigations, Geodesy and Heat Transport) Discovery Program mission will deploy in 2018 a lander equipped with geophysical and meteorological sensors on the Martian surface (Banerdt *et al.*, 2013), including a single three-component ultra-sensitive very-broadband (VBB) seismometer (Lognonné *et al.*, 2012, 2015). Objectives of the InSight mission are (1) to determine 1D models of Mars' mantle and core to within ±5% uncertainty in seismic-wavespeeds, as well as 3D velocity models of the crust, and (2) to measure the activity and distribution of seismic events on Mars, including both tectonic and impact seismicity (Banerdt *et al.*, 2013). InSight launched successfully on 5 May 2018 and will land on Mars on 26 November 2018. A nominal operation for one Martian year is anticipated, corresponding to roughly two Earth years.

Without plate tectonics, we expect secular cooling as the driver of sustainable tectonic stress on Mars (Phillips, 1991). Theoretical models for thermoelastic cooling (Phillips, 1991; Knapmeyer *et al.*, 2006; Plesa *et al.*, 2018) and observed surface faults (Golombek *et al.*, 1992; Golombek, 2002) predict an occurrence of 4–40 globally detectable marsquakes per

*Also at Swiss Seismological Service (SED), ETH Zürich, Sonneggstrasse 5, 8092 Zurich, Switzerland.

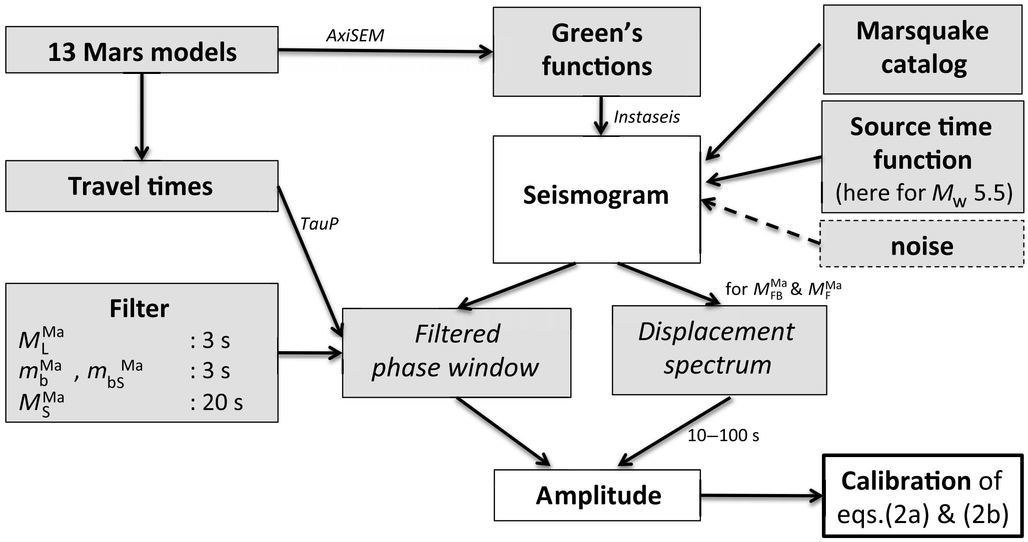

Figure 1. Calibration of magnitude scales for Mars from synthetic seismograms using a suite of structural 1D models. See the Data and Methods section for details.

Martian year, which are estimated to a (body-wave magnitude) m_b 4 event on the Earth. Another source of seismic events on Mars is meteorite impacts. Daubar *et al.* (2015) and Teanby (2015) predict 0.1–30 regional, respectively, ~8–16 InSight-detectable impacts per Martian year. Lognonné and Johnson (2007) predict about 10 impacts per year generating amplitudes exceeding 3×10^{-9} m/s^2.

The Marsquake Service (MQS), as a part of the InSight SEIS Team, is in charge of identification and characterization of seismicity on Mars, as well as management of the seismic-event catalog. The Mars Structure Service is responsible for the determination of 1D and 3D structural models (Panning *et al.*, 2017). In preparation for the data return, a series of single-station event location methods (Panning *et al.*, 2015; Böse *et al.*, 2017) and iterative inversion techniques (Khan *et al.*, 2016; Panning *et al.*, 2017) have been developed and tested (Clinton *et al.*, 2017). In this article, we calibrate magnitude-scaling relations for marsquakes for the MQS that incorporate the state-of-the-art knowledge on Mars' interior structure and the expected ambient and instrumental noise.

Magnitudes characterize the relative size of a marsquake based on the measurements of peak wave amplitudes of a particular phase and frequency recorded by a seismometer and corrected for the attenuation with distance and possibly depth (e.g., Båth, 1981; Kanamori, 1983). The most commonly used scales on the Earth are the (1) local magnitude M_L also known as Richter magnitude (Richter, 1935), (2) body-wave magnitude m_b, (3) surface-wave magnitude M_s (Gutenberg, 1945), and (4) moment magnitude M_w (Hanks and Kanamori, 1979). The first three scales have limited range of applicability and do not satisfactorily measure the size of the largest marsquake source because of amplitude saturation in the narrow frequency ranges they are determined in. The M_w scale, which is based on the concept of the seismic moment M_0 and as such is physically meaningful, applies to all earthquake sizes, but is usually more difficult to compute, especially in a single-station inversion.

Existing Earth-magnitude scaling relations cannot be easily adopted to Mars because the two planets have different interior properties and planet sizes and therefore different amplitude–distance relations. Furthermore, InSight is going to deploy a single seismometer on Mars, so there is a need to define magnitude scales for various seismic phases that may be identified and which are applicable to marsquakes from local to teleseismic distances. In this article, we calibrate magnitude scales for Mars by the simulation of seismic-wave propagation through a set of realistic 1D Mars models. We anticipate these relations to be applied to the initial seismic-event catalog that will be produced by InSight. Depending on the observed attenuation, scattering, and 3D effects, these relations may need to be updated once observational data and new models become available.

Data and Methods

Despite the theoretical studies of Goins and Lazarevicz (1979) on magnitude-dependent detection thresholds, no marsquake signal could be identified in the seismic recordings of the Viking missions in the mid-1970s (Anderson *et al.*, 1977). In the absence of seismic data, we calibrate our magnitude scales with synthetic waveforms that incorporate the current knowledge on Mars interior structure and the expected ambient and instrumental noise. Our procedure is outlined in Figure 1 and will be described in the following.

Mars Structural Models and Travel Times

We use a series of 13 published 1D structural models of Mars' interior (Fig. 2) as described by Clinton *et al.* (2017) and Panning *et al.* (2017) that combine structural models from Rivoldini *et al.* (2011) and Khan *et al.* (2016). These

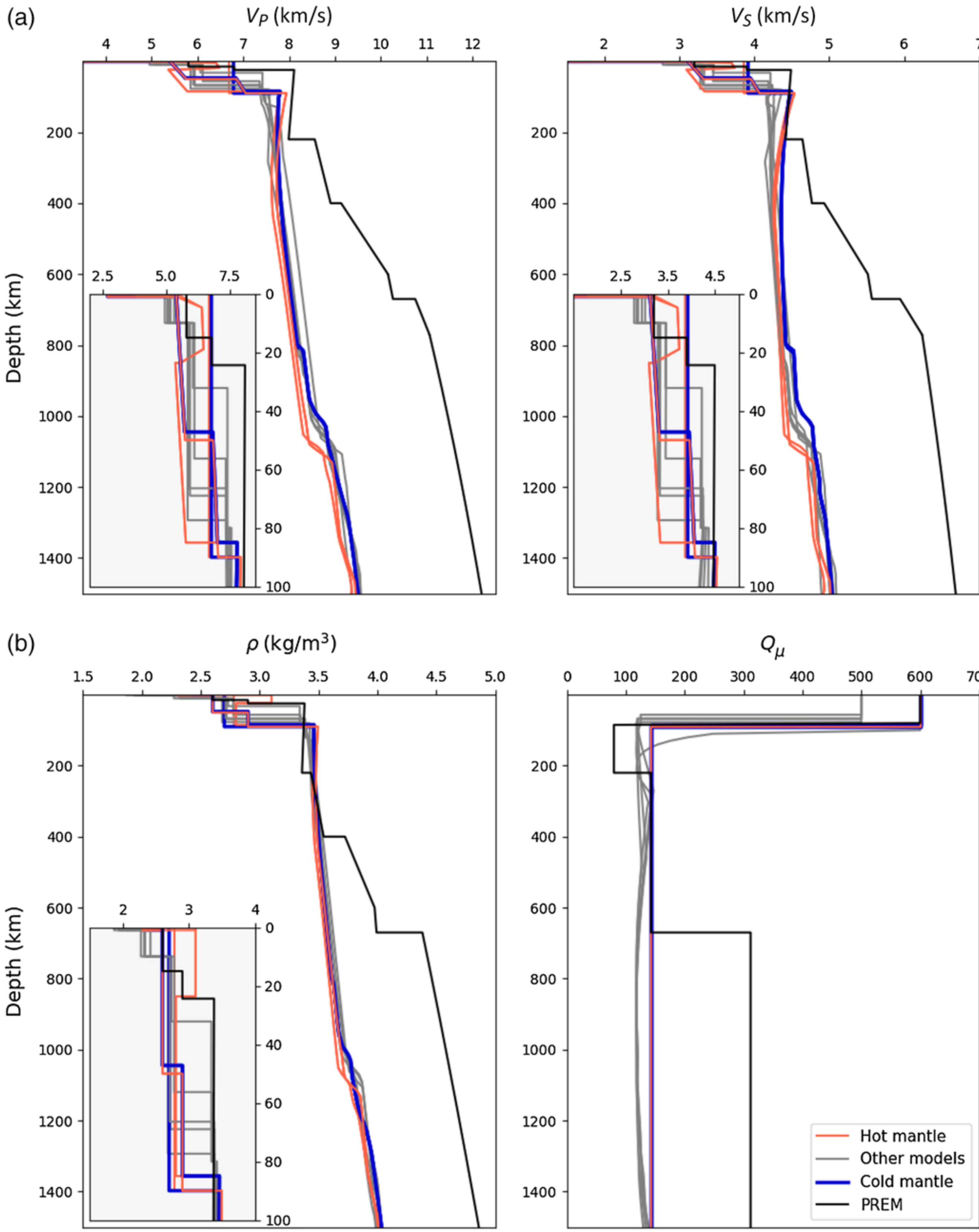

Figure 2. (a) 13 1D Mars models for P- and S-wave velocities V_P and V_S, (b) density ρ, and attenuation Q_μ, used for waveform simulations in this study. Preliminary reference Earth model (PREM) (Dziewonski and Anderson, 1981) is shown for comparison. The color version of this figure is available only in the electronic edition.

Table 1
Parameters and Regression Results for the Six Magnitude Scales

Scale M_i^{Ma}	Amplitude A_i, Band-Pass Filter (BP)	Phase Time Window	Distance Δ and Depth z Range	Coefficients in Equations (2a) or (2b)			
				a_i	b_i	c_i	σ
$M_{\mathrm{L}}^{\mathrm{Ma}}$	$A = \max(\lvert\mathrm{Z}\rvert)$ (m)	$P1 : (P1 + 150\ \mathrm{s})$	$\Delta \le 10°$				
Shallow	BP: 0.2–0.5 Hz		$0 \le z < 20$ (km)	0.9 [1.7]	0.01 [0.01]	7.7 [7.8]	0.38 [0.44]
Deep			$20 \le z \le 100$ (km)	0.9 [1.7]	—	7.9 [8.0]	
$m_{\mathrm{b}}^{\mathrm{Ma}}$	$A = \max(\lvert\mathrm{Z}\rvert, \lvert\mathrm{N}\rvert, \lvert\mathrm{E}\rvert)$ (m) BP: 0.2–0.5 Hz	$P1 : PP$ or $P1 : S1$ (if PP not existent)	$5° \le \Delta \le 100°$ $0 \le z \le 100$ (km)	1.2 [1.0]	—	9.0 [9.9]	0.48 [0.38]
$m_{\mathrm{b}S}^{\mathrm{Ma}}$	$A = \max(\lvert\mathrm{Z}\rvert, \lvert\mathrm{N}\rvert, \lvert\mathrm{E}\rvert)$ (m) BP: 0.2–0.5 Hz	$S1 : SS$ or $S1 : R1$ (if SS not existent)	$5° \le \Delta \le 100°$ $0 \le z \le 100$ (km)	2.5 [2.1]	—	6.9 [8.4]	0.43 [0.24]
$M_{\mathrm{s}}^{\mathrm{Ma}}$	$A = \max(\sqrt{(\mathrm{E}^2 + \mathrm{N}^2)})$ (m) BP: 0.033–0.066 Hz	$R1$: Rend	$5° \le \Delta \le 180°$ $0 \le z \le 100$ (km)	0.7 [1.1]	0.01 [0.01]	7.9 [7.9]	0.24 [0.16]
$M_{\mathrm{FB}}^{\mathrm{Ma}}$	A from Z$(\mathrm{m}/\sqrt{\mathrm{Hz}})$ BP: 0.01–0.1 Hz	$P1 : R1$	$5° \le \Delta \le 180°$ $0 \le z \le 100$ (km)	1.2 [1.1]	—	8.7 [9.3]	0.35 [0.33]
$M_{\mathrm{F}}^{\mathrm{Ma}}$	A from Z$(\mathrm{m}/\sqrt{\mathrm{Hz}})$ BP: 0.01–0.1 Hz	$P1$: Rend	$5° \le \Delta \le 180°$ $0 \le z \le 100$ (km)	1.1 [1.2]	0.01 [0.01]	7.5 [7.9]	0.29 [0.25]

Amplitude A_i is either the peak amplitude determined from the selected phase time window (for $M_{\mathrm{L}}^{\mathrm{Ma}}$, $m_{\mathrm{b}}^{\mathrm{Ma}}$, $m_{\mathrm{b}S}^{\mathrm{Ma}}$, $M_{\mathrm{s}}^{\mathrm{Ma}}$) or from the low-frequency plateau of the displacement spectrum (for $M_{\mathrm{FB}}^{\mathrm{Ma}}$ and $M_{\mathrm{F}}^{\mathrm{Ma}}$). Selected sensor components, time windows, filters, distance, and depth ranges are given. The fit quality is measured by the standard deviation σ of the error distributions M_i^{Ma}–M_{w}. Numbers in square brackets are calculated from waveform synthetics computed for the preliminary reference Earth model (PREM). Z, N, E sensor components, up–down, north–south, east–west; $P1$, first-arriving P wave; $S1$, first-arriving S wave; $R1$, first surface-wave arrival assuming speed of 4.0 km/s; Rend, last surface-wave arrival assuming speed of 2.5 km/s; PP, free surface reflection of P wave leaving the source downward; SS, free surface reflection of S wave leaving the source downward.

models were constructed to meet the currently available Martian geophysical data, including the mean mass and moment of inertia, as well as tidal response in the form of the second degree tidal Love number and global tidal dissipation. Seismic properties (P and S wavespeeds and density) in the silicate portion of Mars are computed using phase equilibrium computations that self-consistently predict radial profiles of above-mentioned properties as a function of composition, temperature, and pressure (Connolly, 2009). To compute radial shear attenuation profiles, Khan *et al.* (2016) combined the phase equilibrium computations with a laboratory-based viscoelastic dissipation model (Jackson and Faul, 2010). This rheological model, which relies on measurements of anhydrous and melt-free olivine, is both temperature and grain-size sensitive and imposes strong constraints on interior structure (Nimmo and Faul, 2013; Khan *et al.*, 2018). In contrast, the shear attenuation models of Rivoldini *et al.* (2011) were scaled from the preliminary reference Earth model (PREM; Dziewonski and Anderson, 1981). Core properties were calculated using equation-of-state modeling as described in detail by Rivoldini *et al.* (2011). Finally, the Martian mantle compositions used derive from geochemical and isotopic analyses of Martian rocks and primitive solar system material (e.g., Taylor, 2013; Khan *et al.*, 2018). The emphasis here is on producing physically realistic models that incorporate physical constraints derived from thermodynamic considerations and laboratory measurement. We expect that the predicted set of models is representative of our current *a priori* knowledge of Mars' internal structure. Additional modeling uncertainties associated with the attenuation models are examined in the Discussion section.

We apply the TauP-2.4.1 toolbox by Crotwell *et al.* (1999) to predict arrival times of magnitude-relevant phases in each of these models, which we use to cut appropriate time windows for amplitude computations (Ⓔ Fig. S1, available in the electronic supplement to this article). Details on the selected time windows are given in Table 1.

Green's Functions and Waveform Simulations

We compute Green's function (GF) databases for all 13 structural models for source depths down to 100 km with the spectral element code AxiSEM (Nissen-Meyer *et al.*, 2014) at a minimum reliable period of 1 s and for a duration of 30 min, as well as at a minimum of 5 s and for a duration of 60 min. As discussed later, we use the 1 s databases for the calibration of body-wave magnitudes and the longer 5 s databases for the calibration of magnitudes based on surface waves.

We use Instaseis (van Driel *et al.*, 2015) to generate synthetic waveforms from the GFs, assuming a magnitude-dependent source time function (Fig. 3a) that produces an amplitude spectrum of shape $M(f) = 1/(1 + (f/f_c)^2)$. Following Brune (1970), we scale the corner frequency f_c of this spectrum with the seismic moment M_0 as

$$f_c = 0.49 \times V_S \times (\Delta\sigma/M_0)^{1/3} (\mathrm{Hz}), \qquad (1)$$

assuming a stress drop of $\Delta\sigma = 1$ MPa and shear-wave velocity of $V_S = 3$ km/s, which gives $f_c = 1.36$ Hz for

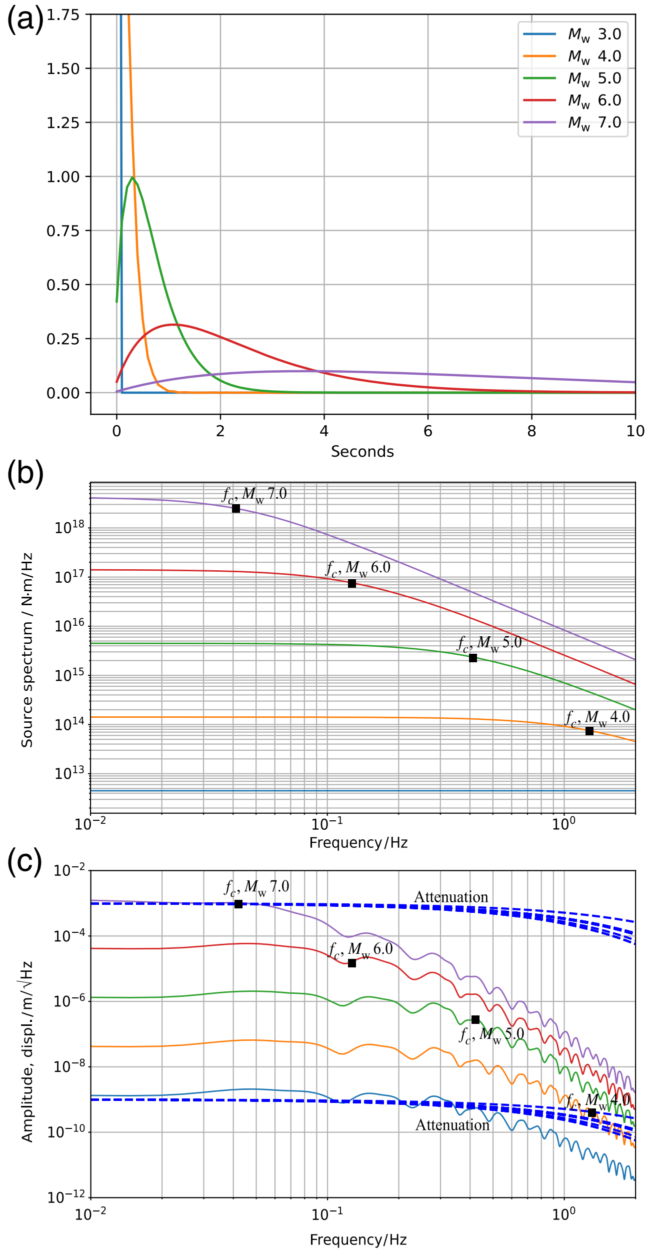

Figure 3. (a) Normalized source time functions and (b) resulting amplitude spectra for $3.0 \leq M_w \leq 7.0$. Corner frequencies f_c are scaled for a stress drop of $\Delta\sigma = 1$ MPa and shear-wave velocity of $V_S = 3.0$ km/s. (c) *P*-wave spectra at 40° distance for the magnitude-dependent source spectrum in (b). The dashed lines in (c) show the attenuation curves, assuming a propagation length of 1400 km, $Q_\kappa = 10{,}000$ and $Q_\mu = 120$–150. The color version of this figure is available only in the electronic edition.

$M_0 = 1.26 \times 10^{15}$ N · m ($M_w = 4.0$, Fig. 3b). The effect of f_c, however, is mostly hidden for marsquakes with magnitudes of $M_w < 5.0$ at larger distances because of the strong attenuation of seismic waves at frequencies above 0.3 Hz as predicted by the Mars models (Fig. 3c). The importance of attenuation at teleseismic distances was noted also by Goins and Lazarewicz (1979), Lognonné and Mosser (1993), and Mocquet (1999).

Noise Models

We determine magnitude-scaling relations in this study from noise-free waveform synthetics. However, we validate these relationships in the presence of realistic noise. The Martian noise model (Fig. 4; Murdoch *et al.*, 2015a,b; Mimoun *et al.*, 2017) considers various noise sources, including the sensors and systems, as well as the environment (fluctuating-pressure-induced ground deformation, magnetic field, and temperature-related noise) and the nearby lander (wind-induced solar panel vibrations). Strongest noise is expected at frequencies below 0.035 Hz (~30 s); at higher frequencies, the predicted noise is about 2 orders of magnitude smaller than on the Earth because of the absence of microseisms, which on the Earth are dominant between 0.025 and 0.5 Hz (2–40 s) (Fig. 4). Because of the absence of oceans, we do not expect a microseismic peak on Mars.

Calibration of Magnitude Scales

Traditional magnitude scales developed for the Earth, such as M_L, m_b, or M_s (as defined, e.g., in the International Association of Seismology and Physics of the Earth's Interior [IASPEI] standards; see Bormann, 2012, chapter 3), cannot be easily adopted to Mars because interior structure of the two planets is very different. Furthermore, we want our magnitude equations to be applicable to the continuous seismic data streams returned from InSight; even though the vertical component will be sampled by default with 10 samples per second, the horizontals will be sampled with only 2 samples per second, which means that magnitude scales (at least those for *S* waves) need to be defined at frequencies below 1.0 Hz.

The InSight mission has the goal to characterize as many marsquakes as possible. Therefore, we define in this study six magnitude scales for various seismic phases. We anticipate that for some of the InSight-detected marsquakes, it will be possible to identify multiple phases and thus to compute multiple magnitude types. We define the following six scales, where we use superscript Ma for Mars: correspondent to the local and body-wave magnitude scales on the Earth, we define for Mars (1) M_L^{Ma}, (2) m_b^{Ma} (for first-arriving *P* wave) and (3) m_{bS}^{Ma} (for first-arriving *S* wave); all three magnitude scales are computed at a period of 3 s using a fourth-order Butterworth band-pass filter with corner frequencies at 0.2 and 0.5 Hz. We also define (4) a surface-wave magnitude for Mars, M_s^{Ma}, which we compute at a period of 20 s (15–30 s band-pass). Finally, we compute the moment magnitudes, (5) M_{FB}^{Ma} and (6) M_F^{Ma}, from the low-frequency (10–100 s) amplitude determined from the displacement spectrum using either body waves or the full record (Fig. 4). As an example, Ⓔ Figure S2 shows the selected time windows and peak values for each magnitude scale for a marsquake simulated at 10° distance.

For magnitude scales without a clear dependence on source depth (m_b^{Ma}, m_{bS}^{Ma}, and M_{FB}^{Ma}), we assume the following log–linear relationship between magnitude M_i^{Ma}, amplitude A_i, and epicentral distance Δ (°)

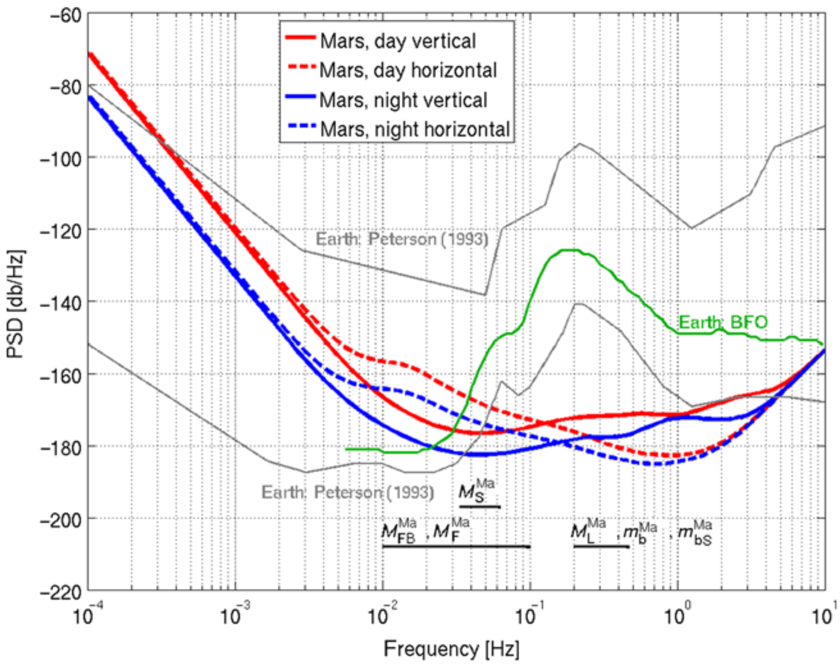

Figure 4. Mars noise model after Murdoch *et al.* (2015a,b) and Mimoun *et al.* (2017) in comparison with typical noise levels on the Earth. For frequencies above 0.035 Hz (30 s) the noise at Black Forest Observatory (BFO), a high-quality Earth station relatively far from the oceans, is significantly higher than what is expected on Mars, but at lower frequencies, this is reversed. We define our magnitude scales for Mars at 3 s (for M_L^{Ma}, m_b^{Ma}, and m_{bS}^{Ma}), at 20 s (for M_s^{Ma}), and at 10–100 s (for M_{FB}^{Ma} and M_F^{Ma}), respectively. The color version of this figure is available only in the electronic edition.

$$M_i^{Ma} = \log_{10}(A_i) + a_i \times \log_{10}(\Delta) + c_i. \quad (2a)$$

For magnitude scales with a strong dependence on source depth z (km) (M_L^{Ma}, M_s^{Ma}, and M_F^{Ma}), we use

$$M_i^{Ma} = \log_{10}(A_i) + a_i \times \log_{10}(\Delta) + b_i \times z + c_i, \quad (2b)$$

in which A_i is either the filtered peak displacement amplitude (m) determined within a certain time window from the waveform time series (for M_L^{Ma}, m_b^{Ma}, m_{bS}^{Ma}, and M_s^{Ma}) or the spectral amplitude ($\mathrm{m}/\sqrt{\mathrm{Hz}}$) determined from the long-period plateau of the amplitude displacement spectrum (for M_{FB}^{Ma} and M_F^{Ma}). Similar to the Earth, we determine A_i for m_b^{Ma} and m_{bS}^{Ma} from the peak amplitude using all three sensor components Z (up–down), N (north–south), and E (east–west); for M_s^{Ma}, we use only horizontal, and for M_L^{Ma}, M_{FB}^{Ma}, and M_F^{Ma} only vertical components. When fully installed, the orientation of the InSight VBB components will be known. Details on the selected filters, waveform components, and time windows for each magnitude scale are given in Table 1.

To determine the coefficients a_i, b_i, and c_i in equations (2a) and (2b), we minimize the magnitude residuals M_i^{Ma}–M_w for a dataset of 2600 randomly distributed marsquakes with random source mechanisms. Relative to the expected limited magnitude range for marsquakes (e.g., Golombek, 2002; Knapmeyer *et al.*, 2006), we chose a fairly large event size for calibration and simulate all events as $M_0 = 2.24 \times 10^{17}$ N · m (M_w 5.5; Kanamori, 1977). We assume an impulsive source because equation (1) predicts a corner frequency above the simulation frequency. Epicenters are chosen to follow a logarithmic distribution in distance to reflect the functional dependencies in equations (2a) and (2b); the event depth varies uniformly from 0 to 100 km (Fig. 5). We model our marsquakes as double-couple events with random—uniformly distributed—strike, rake, and dip. For each simulated event, a single model is randomly selected. Because the length of the GFs in the 1 s databases is limited to 30 min, we use these databases only for the calibration of local and body-wave magnitudes (M_L^{Ma}, m_b^{Ma}, and m_{bS}^{Ma}), and we use the 5 s databases of 60 min duration for the calibration of M_s^{Ma}, M_{FB}^{Ma}, and M_F^{Ma}.

As specified in Table 1, we filter the simulated waveforms and determine A_i from the respective phase time intervals for each magnitude scale (Fig. 1). To avoid problems caused by our epicentral distance metric for deep events at close distances (distance-depth trade-off), we remove prior to the regression all events at epicentral distances of $\Delta < 1°$.

Results

Figure 6 shows the decay of amplitude A_i with epicentral distance Δ for all six magnitude scales. Although the decay is mostly log–linear, there are for some scales subtle changes in the slope at $\Delta \sim 10°$ and $\sim 100°$ caused by peculiarities of crustal and core phases such as shadow zones. Up to a distance of 5°, the seismic-wave propagation occurs mostly in the crust, which makes the amplitudes only weakly dependent on distance. At larger distances, amplitudes are controlled mainly by the attenuation in the mantle, which manifests in a stronger amplitude decay. Based on this observation, we decide to calibrate our magnitude scales for the following distance ranges: (1) M_L^{Ma} for events at $\Delta \le 10°$, (2) m_b^{Ma} and m_{bS}^{Ma} for $5° \le \Delta \le 100°$, and (3) M_s^{Ma}, M_{FB}^{Ma}, and M_F^{Ma} for $5° \le \Delta \le 180°$. As shown later, each magnitude scale actually extends to much larger distance ranges with acceptable errors.

The amplitudes of some phases and frequency bands show a strong dependence on the source depth, with shallow marsquakes generating larger amplitudes at the planet surface than those at greater depths (Fig. 6). To investigate this depth dependence in more detail, we plot in Figure 7 the magnitude residuals M_i^{Ma}–M_w after a pure distance regression using equation (2a): M_L^{Ma} (in particular for shallow events at $z < 20$ km), M_s^{Ma}, and M_F^{Ma} show a clear depth

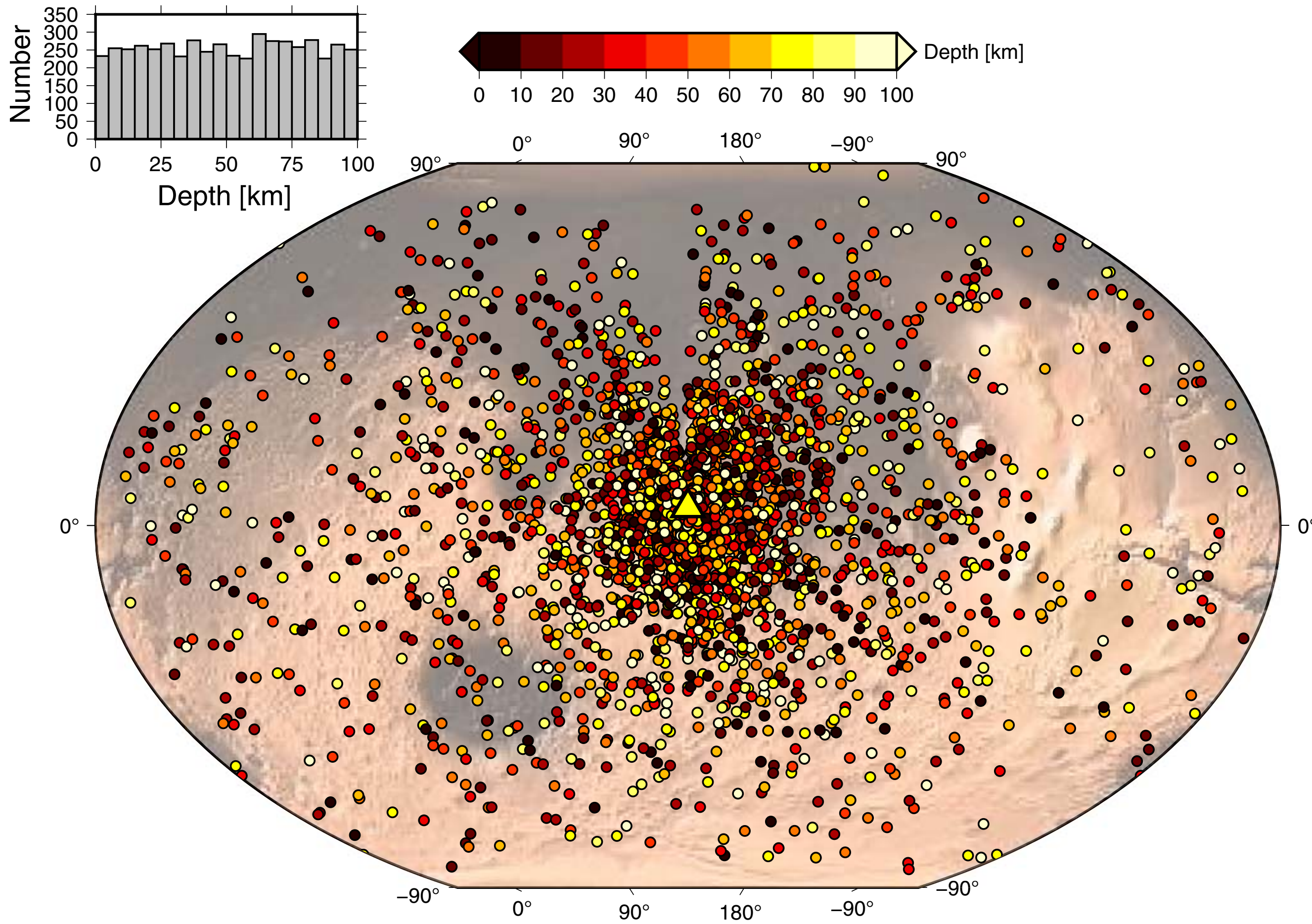

Figure 5. Distribution of synthetic marsquakes for magnitude calibration. Whereas all event magnitudes are simulated as M_{w} 5.5 ($M_0 = 2.24 \times 10^{17}$ N · m), source depths and focal mechanisms are kept random. The color version of this figure is available only in the electronic edition.

dependence, but the depth dependence is weak for $m_{\mathrm{b}}^{\mathrm{Ma}}$, $m_{\mathrm{b}S}^{\mathrm{Ma}}$, and $M_{\mathrm{FB}}^{\mathrm{Ma}}$. This observation is consistent with observations on the Earth (e.g., Eissler and Kanamori, 1986).

After this preliminary assessment, we run a complete amplitude regression in the scale-dependent distance ranges as specified earlier, including both distance and depth dependencies for $M_{\mathrm{L}}^{\mathrm{Ma}}$, $M_{\mathrm{s}}^{\mathrm{Ma}}$, and $M_{\mathrm{F}}^{\mathrm{Ma}}$ using equation (2b), while keeping equation (2a) for $m_{\mathrm{b}}^{\mathrm{Ma}}$, $m_{\mathrm{b}S}^{\mathrm{Ma}}$, and $M_{\mathrm{FB}}^{\mathrm{Ma}}$. For $M_{\mathrm{L}}^{\mathrm{Ma}}$, we use equation (2b) only for shallow events at $z < 20$ km and set $z = 20$ km for all events at greater depth, so that the b_i term effectively adds to the constant c_i.

Table 1 summarizes the regression results for all six magnitude scales. We obtain stable magnitude calibrations with respect to M_{w} 5.5 for all scales with standard deviations σ of the residual distributions M_i^{Ma}–M_{w} ranging from $\sigma = 0.24$ for $M_{\mathrm{s}}^{\mathrm{Ma}}$ to $\sigma = 0.48$ for $m_{\mathrm{b}}^{\mathrm{Ma}}$. With the exception of $M_{\mathrm{L}}^{\mathrm{Ma}}$, which is valid only for local marsquakes at epicentral distances of up to 10°, the $m_{\mathrm{b}}^{\mathrm{Ma}}$ and $m_{\mathrm{b}S}^{\mathrm{Ma}}$ scales can be extended with acceptable errors (usually < 0.5 magnitude units) to distances from 0° to 100°, scales for $M_{\mathrm{s}}^{\mathrm{Ma}}$ and $M_{\mathrm{F}}^{\mathrm{Ma}}$ from 0° to 180°, and for $M_{\mathrm{FB}}^{\mathrm{Ma}}$ from 5° to 180° (Fig. 8).

To calibrate our magnitude scales with the seismic moment magnitude M_{w} over a larger range of magnitudes, we create a second random marsquake dataset of 2600 events for $1.0 \le M_{\mathrm{w}} \le 7.0$ and compare our magnitude estimates with the known moment magnitude of these events (Fig. 9). Because our magnitude scales were computed for different phases in different frequency bands, there is no *a priori* reason for magnitude scales to agree. Magnitudes scales for the Earth also tend to disagree if computed over large magnitude ranges (e.g., Shearer, 1999). The seismic moment represents a long-period end of the source spectrum, so a high correlation of the six magnitudes scales with the seismic moment implies that the entire spectrum is uniquely determined from the long-period end (Kanamori, 1983), which is inconsistent with the observed magnitude-dependent source spectra in equation (1). Our Mars magnitudes $M_{\mathrm{L}}^{\mathrm{Ma}}$, $m_{\mathrm{b}}^{\mathrm{Ma}}$, and $m_{\mathrm{b}S}^{\mathrm{Ma}}$ agree well with M_{w} for $4.0 < M_{\mathrm{w}} < 6.0$; for smaller and larger events, the seismic moment magnitude tends to be underestimated by up to one full magnitude unit or even more (Fig. 9). For $M_{\mathrm{s}}^{\mathrm{Ma}}$, $M_{\mathrm{FB}}^{\mathrm{Ma}}$, and $M_{\mathrm{F}}^{\mathrm{Ma}}$, a good agreement with M_{w} is expected for $5.0 < M_{\mathrm{w}} < 7.0$; smaller events

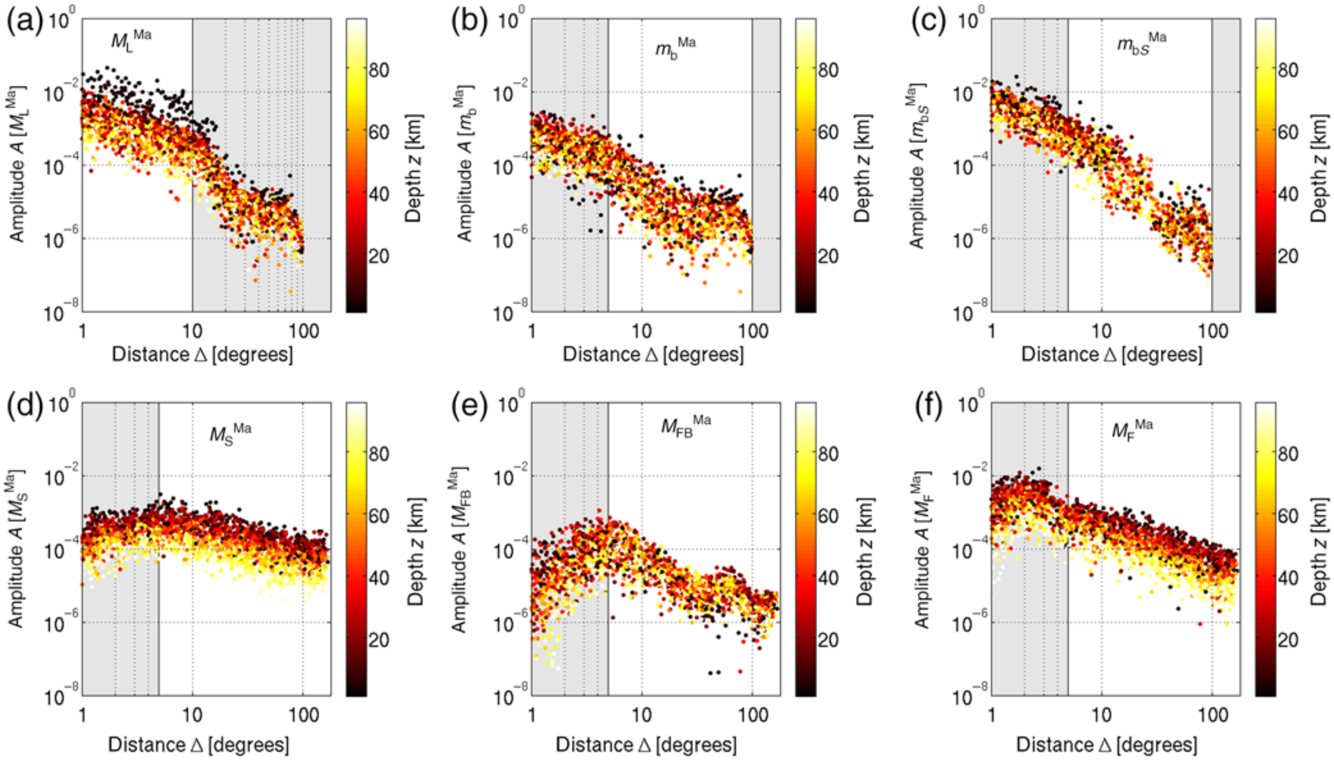

Figure 6. Decay of amplitudes A_i as a function of epicentral distance Δ and source depth z for all six magnitude scales using a set of 2600 synthetic marsquakes (M_w 5.5, $M_0 = 2.24 \times 10^{17}$ N·m). We select the following distance ranges (shown as white-shaded areas) for magnitude calibration: (a) M_L^{Ma}: $\Delta < 10°$, (b) m_b^{Ma}: $5° < \Delta < 100°$, (c) m_{bS}^{Ma}: $5° < \Delta < 100°$, and (d) M_s^{Ma}: $5° < \Delta < 180°$, (e) M_{FB}^{Ma}: $5° < \Delta < 180°$, and (f) M_F^{Ma}: $5° < \Delta < 180°$; local magnitude, M_L^{Ma}, surface-wave magnitude, M_s^{Ma}, and moment magnitude, M_F^{Ma}, show a strong dependence on source depth. Large differences in m_b^{Ma} and m_{bS}^{Ma} are due to the distinct attenuation of P and S waves in the crust and mantle. The color version of this figure is available only in the electronic edition.

tend to be underestimated by up to one full magnitude unit or more. The cause for this systematic bias is discussed in the Discussion section. From piecewise linear regression, we obtain for $M_i^{Ma} = \{M_L^{Ma}, m_b^{Ma}, m_{bS}^{Ma}\}$

$$M_w^{Ma} = 0.1 + M_i^{Ma} + 1/3 \times \Phi(4.5 - M_i^{Ma}) \pm 0.4, \quad (3a)$$

in which $\Phi(x) = \max(x, 0)$, and for $M_i^{Ma} = \{M_s^{Ma}, M_{FB}^{Ma}, M_F^{Ma}\}$

$$M_w^{Ma} = 1.9 + 2/3 \times M_i^{Ma} \pm 0.2. \quad (3b)$$

Equations (3a) and (3b) allow calculating the moment magnitude M_w^{Ma}, from each marsquake magnitude scale M_i^{Ma} (valid over the entire magnitude range from 1.0 to 7.0) as determined from equations (2a) and (2b) using the coefficients in Table 1.

We calibrated our magnitude scales (Table 1) from noise-free waveform synthetics and tested these relations for $1.0 \le M_w \le 7.0$ in the absence of noise (Fig. 9). For a final validation of our scales, we generate a second test dataset of event seismograms for 2600 randomly distributed marsquakes ($1.0 \le M_w \le 7.0$), but this time we superimpose realistic noise. We use the conservative InSight noise model for day (Fig. 4) and add random phase noise time series to the synthetics. As shown in Figure 10, the added noise causes the estimated magnitudes to saturate for small marsquakes ($M_w < 2.0$ for m_b^{Ma} and m_{bS}^{Ma}; $M_w < 2.5$ for M_F^{Ma}; $M_w < 3.0$ for M_s^{Ma}; $M_w < 3.5$ for M_{FB}^{Ma}) for events distances $\Delta > 15°$ (~900 km on Mars), which means that these events are hidden in the Mars background noise and are therefore undetectable. For small marsquakes ($M_w < 3.5$), M_L^{Ma} tends to underestimate M_w and thus M_0.

Discussion

Magnitude scales for earthquakes and marsquakes depend on the decay of seismic-wave amplitudes A with increasing distance, which is controlled by elastic (geometrical spreading, multipathing, and scattering attenuation) and anelastic (intrinsic attenuation) processes: whereas elastic processes conserve the energy in the propagating wavefield, anelasticity converts seismic energy to heat. The 1D structural Mars models and AxiSEM waveform simulations used in this study account for both geometrical spreading and anelastic attenuation but neglect scattering and multipathing through 3D structures.

The strongest decay of amplitudes in our synthetics is caused by the geometrical spreading. By conservation of energy, the energy in a unit area of the growing wavefront decreases as r^2, in which r is the distance from the source.

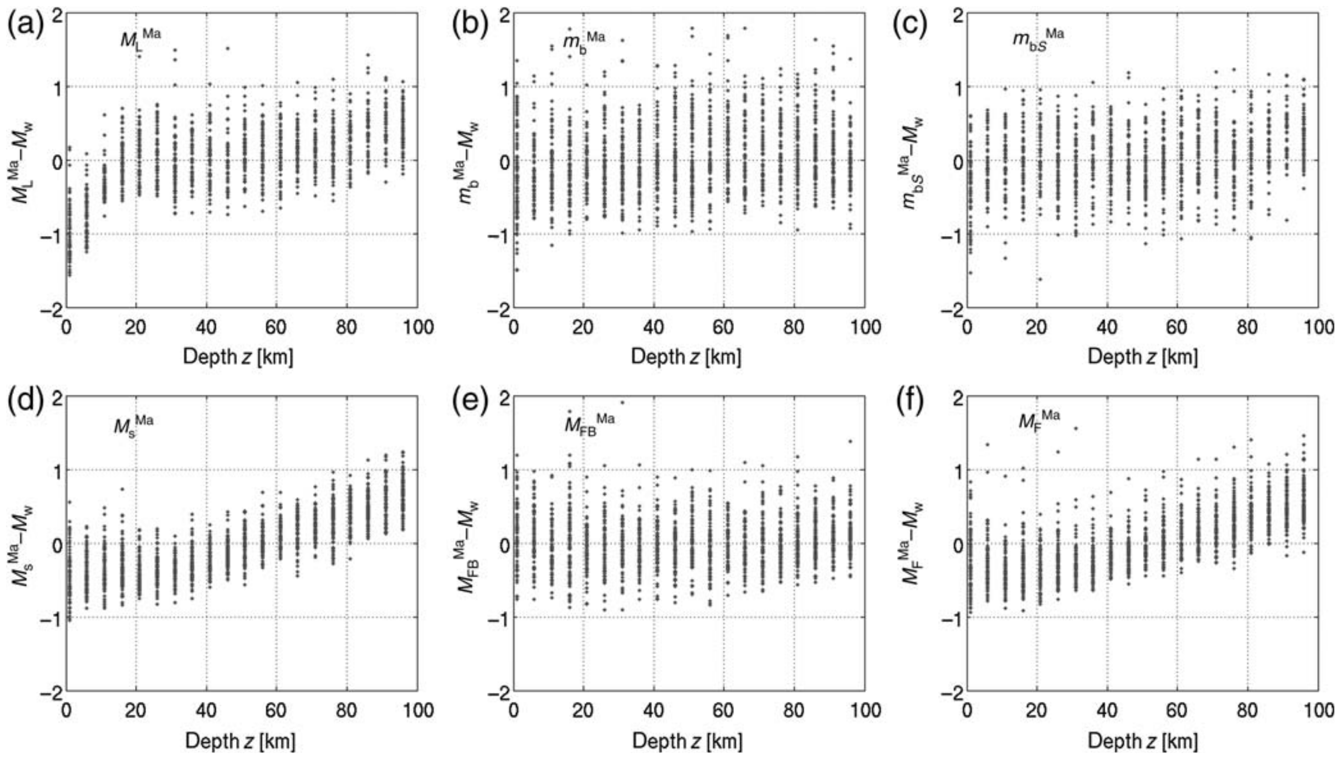

Figure 7. Magnitude residuals after pure distance regression using equation (2a). The residuals are strongly depth dependent for (a) M_L^{Ma} (in particular for shallow events at $z < 20$ km), (d) M_s^{Ma}, and (f) M_F^{Ma}, but the depth dependence is weak for (b) m_b^{Ma}, (c) m_{bS}^{Ma}, and (e) M_{FB}^{Ma}.

Body-wave amplitudes hence decay with $1/r$, so we expect $\log_{10}(A)$ to decrease by about one unit per unit change in $\log_{10}(\Delta)$ (Fig. 6), which would correspond to $a_i \approx 1$ in equations (2a) and (2b) (Table 1). The decay of surface-wave amplitudes is more complex, also because of their dispersion.

Our marsquake synthetics were computed for radial 1D models. In reality, body waves travel through inhomogeneous 3D structures, which cause amplitudes to increase and decrease because of the focusing and defocusing of seismic rays, respectively. It is expected that lateral structural variations in the Martian crust are strong (Larmat *et al.*, 2008; Bozdag *et al.*, 2017), which manifests as a crustal dichotomy between the southern and northern hemispheres (e.g., Zhong and Zuber, 2001): the crust in the northern lowlands with an estimated average thickness of ~30 km is only half as thick as in the southern highlands. We expect 3D effects to increase the variability of the waveform amplitudes and thus to lead to a greater spread in the estimated magnitudes compared with the results from our 1D models.

Intrinsic attenuation on Mars is not known well. Khan *et al.* (2018) estimate that Q_μ is between 120 and 200 at seismic periods in the upper mantle, which is consistent with the model suite that we have been using for our magnitude calibration in this article. The magnitude estimate change ΔM depends on ΔQ as

$$\Delta M = \frac{\partial M}{\partial Q}\Delta Q = \frac{\pi f r}{c \ln 10} Q_0^{-2} \Delta Q. \tag{4}$$

Assuming that Q in the upper mantle varies around $Q_0 = 150$, the magnitude estimated from an S wave at $r = 2000$ km distance depends on Q by $(\partial M/\partial Q) = 8 \times 10^{-3}$. Therefore, even a change in attenuation by 1/3, that is, $\Delta Q = \pm 50$, results only in a $\Delta M = \pm 0.3$. Local waves that travel mainly through the crust, in which Q is expected being much larger (assume $Q_0 = 600$ and $r = 500$ km), are even less sensitive with $(\partial M/\partial Q) = 1.4 \times 10^{-4}$, so that even $\Delta Q = 100$ results in small magnitude uncertainties compared with those introduced by the focal mechanism, the depth, and uncertainties in the velocity model. The effect is even smaller for other magnitude scales because they are measured at lower frequencies or for P waves, which are less affected by attenuation.

Goins *et al.* (1981) developed magnitude and energy equations for moonquakes that account for the effects of intense scattering on the Moon. On Mars, we expect diffusive scattering to be less pronounced because strong scattering requires extreme low-volatile conditions (for very high Q), which are not expected on Mars (Banerdt *et al.*, 2013).

To compare our magnitude-scaling results with calibrations for the Earth, we repeat the amplitude regression for terrestrial waveforms for a similar seismic-event catalog. The waveforms are simulated with AxiSEM for the (anisotropic) PREM of Dziewonski and Anderson (1981). The corresponding GF database *prem_a_2s* is hosted at the Incorporated Research Institutions for Seismology (IRIS, Krischer *et al.*, 2017; see Data and Resources). These GFs were

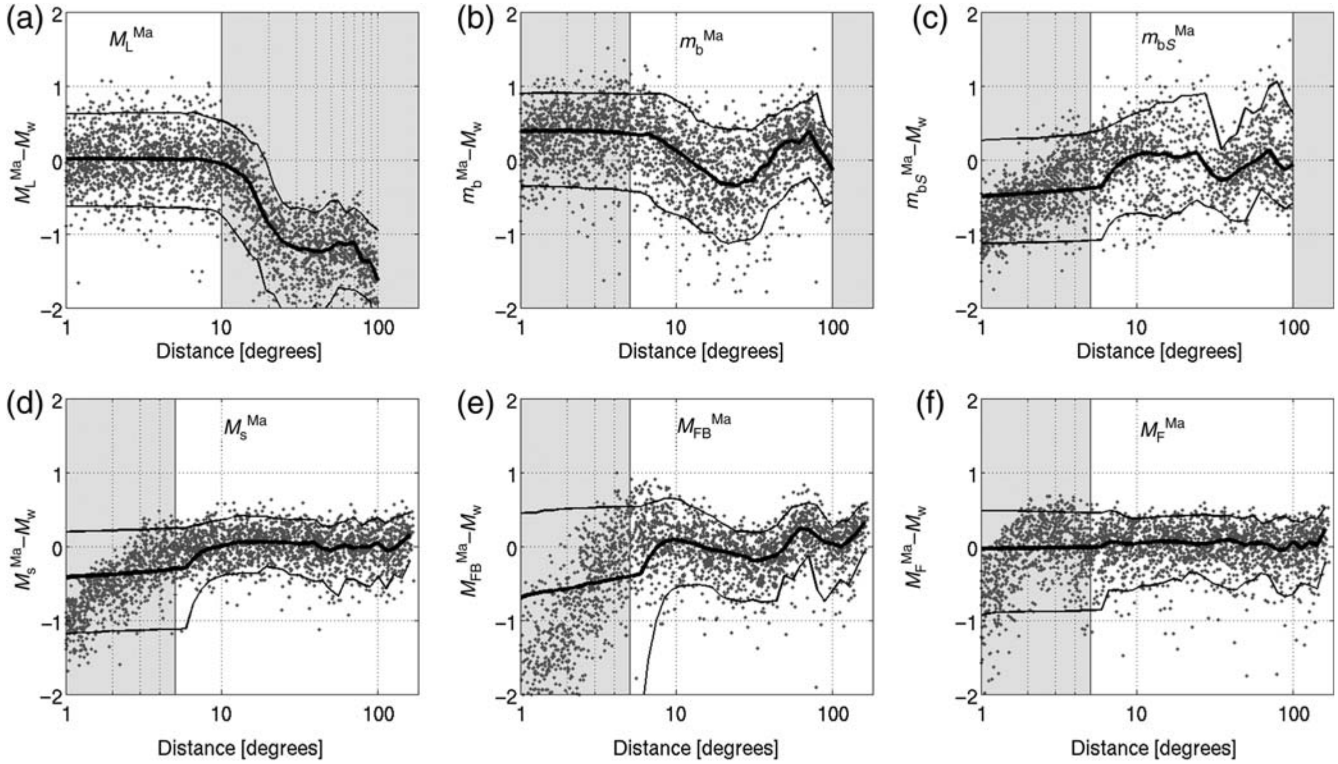

Figure 8. (a–f) Magnitude residuals as a function of epicentral distance for all six scales. With the exception of M_L^{Ma} in (a), which is valid only for local marsquakes at epicentral distances of $\Delta < 10°$, all other scales are usable for events up to 100° or even up to 180°. Extending the magnitude relations to larger distances increases the magnitude errors with tolerable errors. Thick black lines show median values, and thin black lines show the 5th and 95th percentiles. Only white-shaded distance ranges were considered for magnitude calibration.

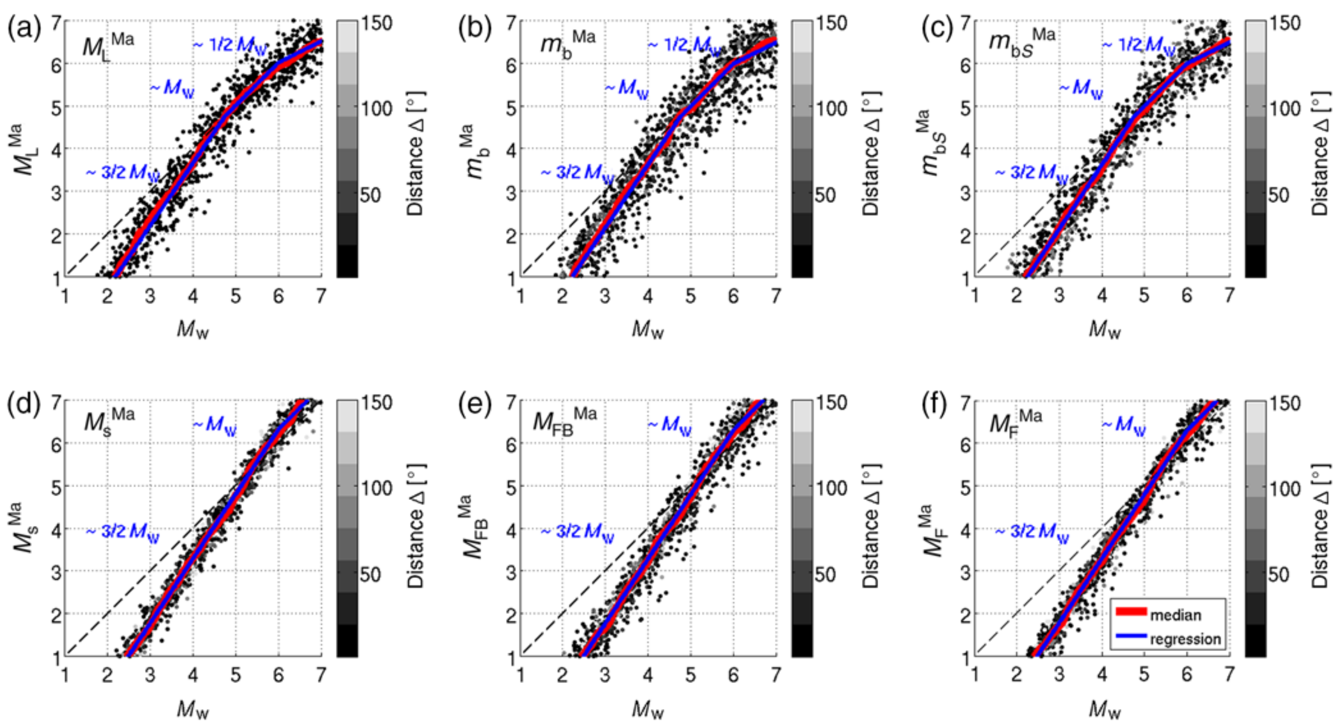

Figure 9. Comparison of the six magnitude scales (a–f) with moment magnitude M_w without noise. M_L^{Ma}, m_b^{Ma}, and m_{bS}^{Ma} agree well with M_w for $4.0 < M_w < 6.0$; for smaller and larger events M_w tends to be underestimated by up to one full magnitude unit or even more. For M_s^{Ma}, M_{FB}^{Ma}, and M_F^{Ma}, a good agreement with M_w is expected for $5.0 < M_w < 7.0$; smaller events tend to be underestimated by up to one full magnitude unit or more. The color version of this figure is available only in the electronic edition.

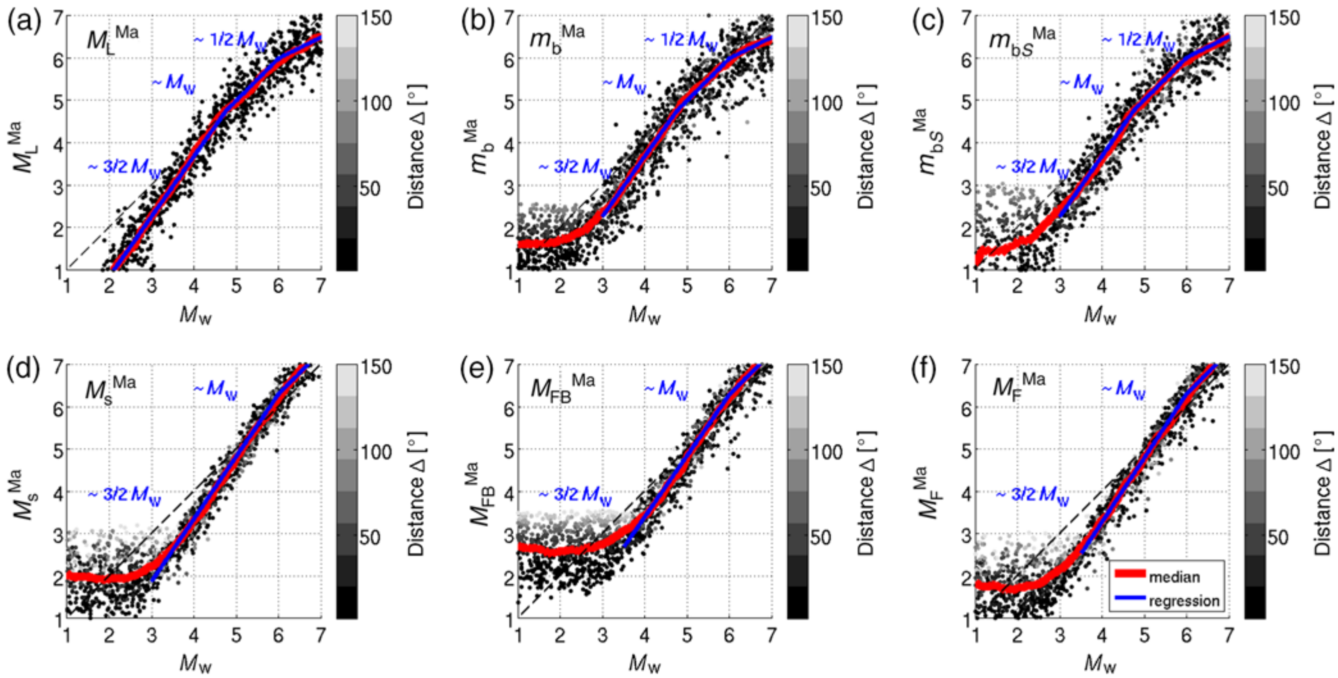

Figure 10. Validation of our magnitude relations (a–f) in the presence of realistic noise. The added noise causes the estimated magnitudes to saturate for small marsquakes ($M_w < 3.0$) at large distances ($\Delta > 15°$, ~900 km on Mars), which means that these events are hidden in the Mars background noise and are hence undetectable. The color version of this figure is available only in the electronic edition.

computed at 2 s; we were using 1 s GFs for Mars. The results from magnitude calibration for the Earth are shown in Table 1 and Ⓔ Figures S3–S5. Most of our magnitude scales are defined differently (in terms of frequency) than in the standard Earth magnitude relations (e.g., Bormann, 2012). The surface-wave magnitude M_s, however, is defined at 20 s both in our relationship and in the IASPEI reference (e.g., Bormann, 2012, chapter 3). We find that our scaling coefficient a_i determined from the PREM waveform simulations is with $a_i = 1.1$ (Table 1) significantly smaller than in the IASPEI reference as well as in the original publication by Gutenberg (1945), in which $a_i = 1.66$. As pointed out by several authors (e.g., von Seggern, 1977; Herak and Herak, 1993; Rezapour and Pearce, 1998; Bormann, 2012), the IASPEI reference relation, however, suffers from a systematic distance-dependent bias because it had been developed for calibrating $(A/T)_{max}$ over a wide range of periods and distances rather than for calibrating displacement amplitudes A at periods of $T \approx 20$ s. To overcome this bias, Herak and Herak (1993) proposed an alternative M_s relation at 20 s, which holds for $4° < \Delta < 180°$. In this relation, the scaling coefficient is $a_i = 1.1$, which is in excellent agreement with our findings (Table 1) and which is also consistent with relations by von Seggern (1977). The relation by Herak and Herak (1993) has no depth-dependent coefficient but is averaged over earthquakes of different source depths. Our M_s relation for the Earth agrees well with Herak and Herak (1993) for $z = 60$ km (Ⓔ Fig. S6).

Both the distance- and depth-dependent coefficients a_i and b_i in our magnitude relations (Table 1) are quite similar for Mars and Earth even though the distant-dependent decay of amplitudes, in particular for M_L, is generally smaller on Mars (Ⓔ Fig. S6). This effect is likely due to the smaller velocities and densities in the Martian crust and upper mantle (Fig. 2). An exemption is m_b, for which the amplitudes undergo a stronger attenuation than on the Earth. The main difference in our magnitude relations for Mars and Earth is in the constant c_i, which is up to 1.5 units larger on Mars (Table 1). This means that the amplitudes for the same marsquake size are generally greater on Mars (Ⓔ Fig. S6). This discrepancy can be largely attributed to the difference in the planet size: the Earth radius is 1.88 times larger than Mars, so we expect c_i to be $\log_{10}(1.88) \approx 0.3$ times larger on the Earth.

Cross calibration of various magnitude scales on the Earth does not achieve an agreement over a large range of magnitudes (e.g., Shearer, 1999). This is because the Earth magnitude scales are computed for various phases in different frequency bands (on the Earth, M_L is typically calculated at 0.1–3 s, m_b at ~1 s, M_s at ~20 s, and M_w typically at $10 - \infty$ s), so there is no *a priori* reason for magnitude scales to agree. Grouping magnitude scales according to the frequency bands they use actually reaches a much better interscale agreement (Kanamori, 1983). Our marsquake magnitude scales also reach a good agreement with M_0 and M_w for limited magnitude ranges only. For M_L^{Ma}, m_b^{Ma}, and m_{bS}^{Ma}, which we defined at 3 s, we observe $M_i^{Ma} \propto 3/2 \times M_w$ for $M_w < 4.5$, and $M_i^{Ma} \propto M_w$ for $M_w \geq 4.5$. For M_s^{Ma}, M_{FB}^{Ma}, and M_F^{Ma}, which we defined at 10–100 s, we observe $M_i^{Ma} \propto 3/2 \times M_w$ for

$1.0 \le M_w \le 6.0$ (see equations 3a and 3b and Fig. 9). A similar break in 1:1 scaling for small earthquakes is observed on the Earth and is explained by Deichmann (2017) by the observation that the pulse width and equivalently corner frequencies remain practically constant for small earthquakes. Thus, the signals of small earthquakes in an attenuating medium essentially form the impulse response of the medium, which is scaled by the seismic moment. Because we do not expect large marsquakes ($M_w > 5.5$) to occur on Mars (Knapmeyer *et al.*, 2006), magnitude saturation will likely not be an issue, at least not for frequencies below 1 Hz.

The L1 requirements of the InSight Mars mission demand marsquakes to be located with an accuracy of $\pm 25\%$ (L1-SCI-51; Banerdt *et al.*, 2013). As can be seen from Table 1, location uncertainties on this order translate into errors of ± 0.1 to ± 0.3 in magnitude on all six scales, calculated as $\max([|a_i \times \log_{10}(0.75)|, \quad a_i \times \log_{10}(1.25)])$, respectively. With the probabilistic framework developed by Böse *et al.* (2017), location errors for well-locatable events are expected to be smaller than $\pm 25\%$, implying that magnitude uncertainties due to errors in Δ are negligible. More critical are errors in the estimated source depth z, which we expect to be large in the single-station-based locations of the InSight mission. An error of 20 km in z leads to a magnitude increase or decrease by 0.2 units (calculated as $20 \times b_i$) for M_L^{Ma} (shallow events with $z < 20$ km), M_s^{Ma}, M_{FB}^{Ma}, and M_F^{Ma}. Assuming a wrong depth, particularly for very close events at $\Delta < 1°$ (~50 km on Mars) for which the hypocentral instead of the epicentral distance metric should be used, can lead to noticeable magnitude errors. However, observing such a close event during the 2-yr Mars InSight mission is quite unlikely, in particular because most observed surface faults are located at larger distance from the InSight landing site (Knapmeyer *et al.*, 2006).

Conclusions

In this study, we calibrated magnitude scales for marsquakes from synthetic waveform data that incorporate the state-of-the-art knowledge on Mars' interior structure and the expected ambient and instrumental noise of the VBB InSight seismometer. We determined six magnitude scales for marsquakes: M_L^{Ma}, m_b^{Ma}, m_{bS}^{Ma}, M_s^{Ma}, M_{FB}^{Ma}, and M_F^{Ma}, which allow us to compute magnitudes for various identified phases. For each magnitude scale, we provide an approved distance cutoff, but we demonstrate that the relations can be extended to larger distances with acceptable magnitude errors with respect to M_w (Fig. 8).

With the exception of m_b, we expect on Mars a weaker decay of seismic-wave amplitudes with increasing epicentral distance compared with the Earth, mostly due to the lack of a lower mantle, where attenuation on the Earth is strong and also because of the smaller planet size of Mars.

We anticipate that our magnitude relations will be applied to the initial seismic-event catalog produced by InSight. Depending on the observed scattering and 3D effects, these relations may need to be updated when new models become available.

Data and Resources

The Green's function (GF) databases we use here to calibrate our magnitude scales for Mars are publicly available via an HTTP webservice at http://instaseis.ethz.ch/marssynthetics (last accessed June 2018). Readers are referred to Ceylan *et al.* (2017) for more information on extracting waveforms from these databases, as well as 16 pre-existing ones. The *prem_a_2s* GF database for the (anisotropic) preliminary reference Earth model (PREM) is hosted at http://ds.iris.edu/ds/products/syngine (last accessed November 2017).

Acknowledgments

This is InSight (Interior exploration using Seismic Investigations, Geodesy and Heat Transport) Contribution Number 44. M. v. D. was supported by grants from the Swiss National Science Foundation-Agence Nationale Recherche (SNF-ANR project 157133 Seismology on Mars). Computations were done at the Swiss National Supercomputing Center (CSCS) under project ID sm682. The authors would like to thank Associate Editor Allison Bent and Editor-in-Chief Thomas Pratt, as well as three anonymous reviewers for their great comments, which helped improve our article.

References

Anderson, D. L., W. F. Miller, G. V. Latham, Y. Nakamura, M. N. Toksöz, A. M. Dainty, F. K. Duennebier, A. R. Lazarewicz, R. L. Kovach, and T. C. D. Knight (1977). Seismology on Mars, *J. Geophys. Res.* **82,** 4524–4546.

Banerdt, W. B., S. Smrekar, P. Lognonné, T. Spohn, S. W. Asmar, D. Banfield, L. Boschi, U. Christensen, V. Dehant, W. Folkner, *et al.* (2013). InSight: A discovery mission to explore the interior of Mars, *Lunar and Planetary Science Conference, Lunar and Planetary Institution. Technical Report*, Vol. 44, 1915 pp.

Båth, M. (1981). Earthquake magnitude—Recent research and current trends, *Earth Sci. Rev.* **17,** no. 4, 315–398, doi: 10.1016/0012-8252(81)90014-3.

Bormann, P. (Editor) (2012). *New Manual of Seismological Observatory Practice (NMSOP-2)*, IASPEI, GFZ German Research Centre for Geosciences, Potsdam, Germany, doi: 10.2312/GFZ.NMSOP-2.

Böse, M., J. Clinton, S. Ceylan, F. Euchner, M. van Driel, A. Khan, D. Giardini, P. Lognonné, and W. B. Banerdt (2017). A probabilistic framework for single-station location of seismicity on Earth and Mars, *Phys. Earth Planet. In.* **262,** 48–65, doi: 10.1016/j.pepi.2016.11.003.

Bozdağ, E., Y. Ruan, N. Metthez, A. Khan, K. Leng, M. van Driel, M. Wieczorek, A. Rivoldini, C. S. Larmat, D. Giardini, *et al.* (2017). Simulation of seismic wave propagation on Mars, *Space Sci. Rev.* doi: 10.1007/s11214-017-0350-z.

Brune, J. N. (1970). Tectonic stress and the spectra of seismic shear waves from earthquakes, *J. Geophys. Res.* **75,** no. 26, 4997–5009, doi: 10.1029/JB075i026p04997.

Ceylan, S., M. van Driel, F. Euchner, A. Khan, J. Clinton, L. Krischer, M. Böse, S. Stähler, and D. Giardini (2017). From initial models of seismicity, structure and noise to synthetic seismograms for Mars, *Space Sci. Rev.* doi: 10.1007/s11214-017-0380-6.

Clinton, J. F., D. Giardini, P. Lognonné, B. Banerdt, M. van Driel, M. Drilleau, N. Murdoch, M. Panning, R. Garcia, D. Mimoun, *et al.* (2017). Preparing for InSight: An invitation to participate in a blind test for Martian seismicity, *Seismol. Res. Lett.* **88,** no. 5, 1290–1302, doi: 10.1785/0220170094.

Connolly, J. A. D. (2009). The geodynamic equation of state: What and how, *Geochem. Geophys. Geosys.* **10,** no. 10, 1525–2027, doi: 10.1029/2009GC002540.

Crotwell, H. P., T. J. Owens, and J. Ritsema (1999). The TauP Toolkit: Flexible seismic travel-time and ray-path utilities, *Seismol. Res. Lett.* **70,** 154–160.

Daubar, I. J., M. P. Golombek, A. S. McEwen, S. Byrne, M. Kreslavsky, N. C. Schmerr, M. E. Banks, P. Lognonné, T. Kawamura, and F. Karakostas (2015). Measurement of the current Martian cratering size frequency distribution, predictions for and expected improvements from InSight, *46th Lunar and Planetary Science Conference*, 2468 pp.

Deichmann, N. (2017). Theoretical basis for the observed break in M_L/M_w scaling between small and large earthquakes, *Bull. Seismol. Soc. Am.* **107,** no. 2, 505–520, doi: 10.1785/0120160318.

Dziewonski, A., and D. L. Anderson (1981). Preliminary reference Earth model, *Phys. Earth Planet. In.* **25,** no. 4, 297–356, doi: 10.1016/0031-9201(81)90046-7.

Eissler, H. K., and H. Kanamori (1986). Depth estimates of large earthquakes on the island of Hawaii since 1940, *J. Geophys. Res.* **91,** no. B2, 2063–2076.

Goins, N. R., and A. R. Lazarewicz (1979). Martian seismicity, *Geophys. Res. Lett.* **6,** 368–370, doi: 10.1029/GL006i005p00368.

Goins, N. R., A. M. Dainty, and M. N. Toksöz (1981). Seismic energy release of the Moon, *J. Geophys. Res.* **86,** no. B1, 378–388, doi: 10.1029/JB086iB01p00378.

Golombek, M. P. (2002). A revision of Mars seismicity from surface faulting, *33rd Annual Lunar and Planetary Science Conference*, Houston, Texas, 11–15 March 2002, Abstract 1244.

Golombek, M. P., W. B. Banerdt, K. L. Tanaka, and D. M. Tralli (1992). A prediction of Mars seismicity from surface faulting, *Science* **258,** 979–981.

Gutenberg, B. (1945). Amplitudes of surface waves and magnitudes of shallow earthquakes, *Bull. Seismol. Soc. Am.* **35,** 3–12.

Hanks, T. C., and H. Kanamori (1979). A moment magnitude scales, *J. Geophys. Res.* **84,** 2348–2350.

Herak, M., and D. Herak (1993). Distance dependence of M_s and calibrating function for 20 s Rayleigh waves, *Bull. Seismol. Soc. Am.* **83,** no. 6, 1881–1892.

Jackson, I., and U.-H. Faul (2010). Grainsize-sensitive viscoelastic relaxation in olivine: Towards a robust laboratory-based model for seismological application, *Phys. Earth Planet. In.* **183,** 151–163, doi: 10.1016/j.pepi.2010.09.005.

Kanamori, H. (1977). The energy release in great earthquakes, *J. Geophys. Res.* **82,** 2981–2987, doi: 10.1029/JB082i020p02981.

Kanamori, H. (1983). Magnitude scale and quantification of earthquakes, *Tectonophysics* **93,** 185–199.

Khan, A., C. Liebske, A. Rozel, A. Rivoldini, F. Nimmo, J. A. D. Connolly, A.-C. Plesa, and D. Giardini (2018). A geophysical perspective on the bulk composition of Mars, *J. Geophys. Res.* **123,** no. 2, 575–611, doi: 10.1002/2017JE005371.

Khan, A., M. van Driel, M. Böse, D. Giardini, S. Ceylan, J. Yan, J. Clinton, F. Euchner, P. Lognonné, N. Murdoch, *et al.* (2016). Single-station and single-event marsquake location and inversion for structure using synthetic Martian waveforms, *Phys. Earth Planet. In.* **258,** 28–42, doi: 10.1016/j.pepi.2016.05.017.

Knapmeyer, M., J. Oberst, E. Hauber, E. Wählisch, C. Deuchler, and R. Wagner (2006). Working models for spatial distribution and level of Mars' seismicity, *J. Geophys. Res.* **111,** no. E11, doi: 10.1029/2006JE002708.

Krischer, L., A. R. Hutko, M. van Driel, S. Stähler, M. Bahavar, C. Trabant, and T. Nissen-Meyer (2017). On-demand custom broadband synthetic seismograms, *Seismol. Res. Lett.* **88,** no. 4, 1127–1140, doi: 10.1785/0220160210.

Larmat, C. M., J.-P. Montagner, Y. Capdeville, B. Banerdt, P. Lognonné, and J.-P. Vilotte (2008). Numerical assessment of the effects of the topography and the crustal thickness on the Martian seismograms using the coupled modal solution-spectral elements method, *Icarus* **196,** 78–89, doi: 10.1016/j.icarus.2007.12.030.

Lognonné, P., and C. Johnson (2007). 10.03-Planetary seismology, in *Treatise on Geophysics*, G. Schubert (Editor), Elsevier, Amsterdam, The Netherlands, 69–122, doi: 10.1016/B978-044452748-6.00154-1.

Lognonné, P., and B. Mosser (1993). Planetary seismology, *Surv. Geophys.* **14,** 239–302.

Lognonné, P., W. B. Banerdt, D. Giardini, U. Christensen, D. Mimoun, S. de Raucourt, A. Spiga, R. Garcia, A. Mocquet, M. Panning, *et al.* (2012). InSight and single-station broadband seismology: From signal and noise to interior structure determination, *Lunar and Planetary Science Conference, Lunar and Planetary Institution. Technical Report*, Vol. 43, 1983 pp.

Lognonné, P., W. B. Banerdt, R. C. Weber, D. Giardini, W. T. Pike, U. Christensen, D. Mimoun, J. Clinton, V. Dehant, R. Garcia, *et al.* (2015). Science goals of SEIS, the InSight seismometer package, *46th Lunar and Planetary Science Conference*, LPI Contribution Number 1832, 2272 pp.

Mimoun, D., N. Murdoch, P. Lognonné, K. Hurst, W. T. Pike, J. Hurley, T. Nebut, and W. B. Banerdt (2017). The noise model of the SEIS seismometer of the InSight mission to Mars, *Space Sci. Rev.* doi: 10.1007/s11214-017-0409-x.

Mocquet, A. (1999). A search for the minimum number of stations needed for seismic networking on Mars, *Planet. Space Sci.* **47,** nos. 3/4, 397–409, doi: 10.1016/S0032-0633(98)00126-3.

Murdoch, M., D. Mimoun, P. H. Lognonné, and SEIS Science Team (2015a). SEIS performance model environment document, *Technical Report ISGH-SEIS-JF-ISAE-030*.

Murdoch, M., D. Mimoun, P. H. Lognonné, and SEIS Science Team (2015b). SEIS performance budgets, *Technical Report ISGH-SEIS-JF- ISAE-0010*.

Nimmo, F., and U.-H. Faul (2013). Dissipation at tidal and seismic frequencies in a melt-free, anhydrous Mars, *J. Geophys. Res.* **118,** 2558–2569, doi: 10.1002/2013JE004499.

Nissen-Meyer, T., M. van Driel, S. C. Stähler, K. Hosseini, S. Hempel, L. Auer, A. Colombi, and A. Fournier (2014). AxiSEM: Broadband 3-D seismic wavefields in axisymmetric media, *Solid Earth* **5,** 425–445, doi: 10.5194/se-5-425-2014.

Panning, M. P., E. Beucler, M. Drilleau, A. Moquet, P. Lognonné, and W. B. Banerdt (2015). Verifying single-station seismic approaches using Earth-based data: Preparation for data return from the InSight mission to Mars, *Icarus* **248,** 230–242.

Panning, M. P., P. Lognonné, W. B. Banerdt, R. Garcia, M. Golombek, S. Kedar, B. Knapmeyer-Endrun, A. Mocquet, N. A. Teanby, J. Tromp, *et al.* (2017). Planned products of the Mars structure service for the InSight mission to Mars, *Space Sci. Rev.* **211,** nos. 1/4, 611–650, doi: 10.1007/s11214-016-0317-5.

Peterson, J. (1993). Observation and modeling of seismic background noise, *U.S. Geol. Surv. Tech. Rept. 93-322*, 94 pp.

Phillips, R. J. (1991). Expected rates of Marsquakes, *Scientific Rationale and Requirements for a Global Seismic Network on Mars, LPI Technical Rept. 91–02*, Lunar and Planetary Institute, Houston, Texas, 35–38.

Plesa, A. C., M. Knapmeyer, M. P. Golombek, D. Breuer, M. Grott, T. Kawamura, P. Lognonné, N. Tosi, and R. C. Weber (2018). Present day Mars' seismicity predicted from 3D thermal evolution models of interior dynamics, *Geophys. Res. Lett.* **45,** 2580–2589, doi: 10.1002/2017GL076124.

Rezapour, M., and R. G. Pearce (1998). Bias in surface-wave magnitude M_s due to inadequate distance corrections, *Bull. Seismol. Soc. Am.* **88,** no. 1, 43–61.

Richter, C. F. (1935). An instrumental earthquake magnitude scale, *Bull. Seismol. Soc. Am.* **25,** 1–32.

Rivoldini, A., T. Van Hoolst, O. Verhoeven, A. Mocquet, and V. Dehant (2011). Geodesy constraints on the interior structure and composition of Mars, *Icarus* **213,** no. 2, 451–472, doi: 10.1016/j.icarus.2011.03.024.

Shearer, P. M. (1999). *Introduction to Seismology*, Cambridge University Press, Cambridge, United Kingdom.

Taylor, G. J. (2013). The bulk composition of Mars, *Chem. Erde Geochem.* **73,** no. 4, 401–420.

Teanby, N. A. (2015). Predicted detection rates of regional-scale meteorite impacts on Mars with the InSight short-period seismometer, *Icarus* **256,** 49–62.

van Driel, M., L. Krischer, S. C. Stähler, K. Hosseini, and T. Nissen-Meyer (2015). Instaseis: Instant global seismograms based on a broadband waveform database, *Solid Earth* **6,** 701–717, doi: 10.5194/se-6-701-2015.

von Seggern, D. (1977). Amplitude-distance relation for 20-second Rayleigh waves, *Bull. Seismol. Soc. Am.* **67,** 405–411.

Zhong, S. J., and M. T. Zuber (2001). Degree-1 mantle convection and the crustal dichotomy on Mars, *Earth Planet. Sci. Lett.* **189,** nos. 1/2, 75–84.

Institute of Geophysics, ETH Zürich
Sonneggstrasse 5
8092 Zurich, Switzerland
maren.boese@sed.ethz.ch
domenico.giardini@erdw.ethz.ch
simon.staehler@erdw.ethz.ch
savas.ceylan@erdw.ethz.ch
vandriel@erdw.ethz.ch
amir.khan@erdw.ethz.ch
(M.B., D.G., S.S., S.C., M.v., A.K.)

Swiss Seismological Service (SED), ETH Zürich
Sonneggstrasse 5
8092 Zurich, Switzerland
jclinton@sed.ethz.ch
fabian.euchner@sed.ethz.ch
(J.F.C., F.E.)

Université Paris Diderot
Institute de Physique du Globe de Paris
35 rue Hélène Brion
75205 Paris, France
lognonne@ipgp.fr
(P.L.)

Jet Propulsion Laboratory
California Institute of Technology
M/S 321-B60, 4800 Oak Grove Drive
Pasadena, California 91109
william.b.banerdt@jpl.nasa.gov
(W.B.B.)

Manuscript received 29 January 2018;
Published Online 17 July 2018